Energy 362 (2026) 142171

Contents lists available at ScienceDirect

Energy

journal homepage: www.elsevier.com/locate/energy

Thermally coupled pumped thermal energy storage system for a renewable powered ammonia production: Performance assessment and optimal sizing

Mostafa EsmaeiliShayan [a,*], Giovanni Cirina [a], Mouad Arrad [b], Ammar Mouaky [c], Mario Petrollese [a,**]

[a] Department of Mechanical, Chemical and Materials Engineering, University of Cagliari, Cagliari, Italy
[b] Laboratory of Mining, Metallurgy & Materials Engineering, Department of Chemical Engineering & Energy, Rabat National School of Mines, Hadj Ahmed Cherkaoui Avenue - P.O 753, Agdal, Rabat, Morocco
[c] Green Energy Park, Benguerir, Morocco

ARTICLE INFO

Keywords:
Haber-Bosch process
Carnot battery
Thermal energy storage
Energy recovery
Green ammonia
Optimization approach

ABSTRACT

The paper investigates the ability of a pumped thermal energy storage system, coupled with renewable energy generators, to meet the electrical and thermal demands of an ammonia production plant. A steady-state model of an industrial-scale Haber–Bosch process is first developed to quantify the electrical and thermal energy demands and to identify high-temperature waste heat streams suitable for recovery. A tailored pumped thermal energy storage configuration is then designed and simulated. The storage system performance is characterized through a parametric analysis with respect to the compression ratio and the relative sizing of the charging and discharging power ratings. The resulting performance maps are then embedded into an optimization model for sizing the renewable generation and storage subsystems while minimizing the total system cost. Results show that the optimal configuration is strongly influenced by the maximum allowed share of grid electricity: allowing a 10% grid contribution reduces the total cost by about 50% compared to the fully renewable case and leads to a cost-effective design in which the power rating of the pumped thermal energy storage system in discharging mode is equal to the nominal electrical demand of the ammonia plant, while the charging power is approximately 1.5 times the discharging power. Compared with a reference configuration without pumped thermal energy storage, the proposed system reduces total cost by approximately 3–10%, depending on grid contribution and design parameters.

1. Introduction

Green ammonia, produced via renewable energy-powered electrolysis and the Haber-Bosch process, is a key solution for decarbonizing sectors such as agriculture, shipping, and energy storage by reducing dependence on fossil fuels [1]. In addition to fertilizer production, green ammonia serves as an energy storage medium [2], fuel cell input [3], and green hydrogen carrier [4], aligning with the UN Sustainable Development Goals 7 (Affordable and Clean Energy) and 13 (Climate Action) [5].

The production of green ammonia primarily relies on generating hydrogen via water electrolysis powered by Renewable Energy Sources (RES). This approach avoids greenhouse gas emissions typically associated with conventional steam methane reforming. While advanced electrolysis technologies, such as alkaline electrolyzers, can achieve high efficiencies of up to 70%, the process remains energy-intensive, requiring approximately 9–12 MWh of electricity per ton of ammonia produced [6]. In addition to this substantial electricity demand, the Haber-Bosch process itself imposes further energy requirements due to its high-pressure (150–300 bar) and high-temperature (400–500°C) operation conditions [7]. Previous studies have addressed the optimal design of renewable-powered ammonia production systems, highlighting that optimal coupling of electrolyzers with Haber-Bosch reactors can achieve overall system efficiencies between 60% and 70% [8,

This article is part of a special issue entitled: SDEWES 2025 - Invitation Only published in Energy.

* Corresponding author.
** Corresponding author.
E-mail addresses: mostafa.esmaeili@unica.it (M. EsmaeiliShayan), giovanni.cirina@unica.it (G. Cirina), arrad@enim.ac.ma (M. Arrad), mouaky@greenenergypark.ma (A. Mouaky), mario.petrollese@unica.it (M. Petrollese).

https://doi.org/10.1016/j.energy.2026.142171
Received 9 January 2026; Received in revised form 14 July 2026; Accepted 4 August 2026
Available online 5 August 2026

9]. Wang et al. developed a mixed-integer programming model for off-grid green ammonia production considering the flexibility of the electrolysis and Haber–Bosch sections, showing that flexible operation can reduce curtailment and storage requirements and that an optimized wind–solar mix is essential for cost reduction [10]. Techno-environmental-economic studies carried out by Liang et al. have confirmed that storage and renewable generator sizing strongly affect the cost and environmental performance of green ammonia systems [11]. However, despite this promising integration, defining and implementing a fully renewable-powered green ammonia production process remains a significant challenge [12]. This is mainly due to the intermittent nature of RES, the high and continuous energy demand of the electrolysis and Haber–Bosch processes, and the need for reliable thermal and electrical energy supply to ensure stable operation. Consequently, robust energy storage systems are required to stabilize ammonia production under fluctuating renewable power inputs [13].

Among the various energy storage options, Pumped Thermal Energy Storage (PTES) systems have emerged as a particularly promising solution for large-scale and long-duration applications. PTES offers cost-effective storage, scalability, long cycle life, and flexible power ratings, making it well-suited for buffering intermittent renewable generation and supporting industrial processes such as green ammonia synthesis [14]. PTES systems operate by converting surplus electricity into thermal energy via a heat pump during charging and transforming it back into electricity via a heat engine during discharging. However, standard PTES architectures are typically limited to electric round-trip efficiencies of 50-70% [15]. To improve this, the concept of Thermally Integrated pumped thermal energy storage (TI-PTES) has been proposed, leveraging waste heat or external thermal sources. TI-PTES systems are categorized into “hot TI-PTES” and “cold TI-PTES” [16]. In the former configuration, an external heat source is usually used as the low-temperature heat input of the PTES during heat pump mode, resulting in an increase in the charging coefficient of performance [17]. In the latter configuration, a vapor compression cycle produces sub-ambient cold energy during charging. Consequently, during the discharging phase, the power block operates across an expanded temperature range between the external heat source and the cold reservoir, taking advantage of the reduced temperature level of the heat sink [18]. The external heat sources integrated into TI-PTES systems may range from low-to high-grade temperatures [19]. When thermally integrated with such sources, PTES systems have demonstrated the potential to reach very high apparent round-trip efficiencies [20,21]. For instance, Huang et al. investigated a Joule–Brayton cycle PTES multi-energy system integrated with external heat and cold sources, showing that the system can operate as a multi-energy hub and that the integration of both heat and cold sources can significantly increase the apparent electrical efficiency and coefficient of performance [22]. This confirms the potential of TI-PTES not only as electricity storage devices, but also as flexible systems for managing multiple energy vectors. In this regard, Qi et al. proposed a hybrid system combining carbon dioxide energy storage with power-to-methanol production for combined heating, power and methanol generation [23]. Their results showed that the coupling between energy storage and fuel synthesis can improve material and energy utilization, enhance renewable energy integration and support multi-energy production under fluctuating renewable supply. Similar concepts have also been explored by Marques da Cunha et al. for bio-methanol production integrated with a Brayton-based PTES system, highlighting the possibility of exploiting synergies between thermal storage, process heat integration and renewable fuel production [24].

Ammonia synthesis is also inherently exothermic; therefore, recovering the heat released during ammonia formation can significantly improve system efficiency and reduce external energy demand [25]. Generating electricity from the exothermic heat of the ammonia synthesis reactor is one of the most frequently proposed options in the literature, and can be achieved through various power cycles and integration concepts. For instance, excess heat can be utilized to heat the working fluid in supercritical CO_2 cycles [26] or Kalina cycles [27]. Additionally, waste heat can preheat a fraction of the post-synthesis purge gas prior to its combustion, which then generates hot gases required to drive a combined cycle [28,29]. More recently, Mucci et al. investigated ammonia as an energy carrier and storage medium, including concepts that involve thermal storage [30]. However, these approaches mainly focus on ammonia reconversion to electricity or on the sizing of renewable-powered ammonia systems, rather than on the direct integration of a PTES unit with a continuously operating green ammonia production plant.

Beyond power generation, researchers have investigated alternative applications for the valorization of this exothermic heat. Excess heat was considered to regenerate solvents used in CO_2 capture for urea production; this integration resulted in a 50.54% reduction in energy consumption for the monoethanolamide scrubbing process and a 46.85% decrease in CO_2 capture costs [31]. Another promising alternative involves using waste heat to drive a vapor absorption refrigeration cycle, which has been shown to boost energy and exergy efficiency by 8% and 11%, respectively [27].

These findings reinforce the potential of PTES as a synergistic component in decarbonized and energy-optimized ammonia synthesis systems. However, the thermodynamic integration and optimal design of PTES with the Haber-Bosch process remain underexplored, despite the multiple possible interactions between PTES and ammonia plants reported in Table 1. Existing studies generally focus either on TI-PTES with generic external heat and cold sources, on Carnot battery integration with other power-to-fuel processes, or on the optimal sizing of renewable-powered ammonia plants using conventional storage options. Therefore, a research gap remains in the simultaneous assessment of high-temperature waste heat recovery (WHR) from the Haber–Bosch loop, direct process heat supply from the PTES, electric-to-electric storage operation, and optimal sizing of renewable generators and storage capacities.

Table 1
Potential energy interactions between a PTES system and an ammonia production plant.

Interaction	PTES state	Haber-Bosch Process	Description
Heat	Charge/ Discharge	Waste Heat Recovery	PTES could store thermal energy for later use by utilizing waste heat from exothermic reactions in the Haber-Bosch process.
Heat	Charge/ Discharge	Thermal Energy Supply	PTES could provide stored heat to the Haber-Bosch process, potentially reducing the need for external heating sources and enhancing overall energy efficiency.
Cooling	Charge/ Discharge	Cooling Loops Integration	The Haber-Bosch process's refrigeration cycles could be improved by utilizing PTES to absorb cooling energy, thereby enhancing overall thermal management.
Cooling	Charge	Cooling Energy Supply	PTES could provide cooling to the Haber-Bosch process, assisting in the condensation and separation stages of ammonia production.
Electricity	Charge	Electricity Grid Connection	PTES could store energy by utilizing surplus electricity available at the plant site, such as electricity from on-site renewable energy sources or excess grid power.
Electricity	Discharge	Electricity for Operation	PTES could generate electricity during discharge cycles to power compressors, fans, and auxiliary systems in the Haber-Bosch process.

In this framework, the present work investigates the application of a Brayton PTES system to a fully electrified ammonia production plant supplied by hybrid photovoltaic–wind generation. The PTES unit is conceived not only as a long-term electricity storage system, but also as a flexible provider of high-temperature heat to the Haber–Bosch process, while simultaneously recovering high-grade waste heat from the ammonia synthesis loop. The main novelty of the work lies in the development and assessment of a tailored PTES-assisted renewable energy supply system for green ammonia production, combining detailed process and PTES simulations with an optimal sizing model for renewable generators and storage capacities. This approach allows the impact of PTES inclusion on storage performance, renewable generator sizing, storage capacity and total system cost to be assessed.

2. Materials and methods

The methodology adopted in this work combines process simulation, thermodynamic cycle modelling, renewable generation modelling and optimization to assess the application of a PTES system to a reference ammonia production plant supplied by renewable generators. The system configuration is first introduced, followed by the modelling and optimization workflow and by the detailed description of the ammonia plant, PTES system and optimal sizing problem.

2.1. System configuration

The system configuration shown in Fig. 1 is proposed to guarantee the continuous operation of an industrial-scale ammonia production plant while minimizing the use of fossil-based electricity. The ammonia plant is assumed to operate at nominal capacity 24 h per day, imposing nearly constant electrical and thermal demands throughout the year. To minimize greenhouse gas emissions, the plant is supplied primarily by renewable electricity and by a PTES system, supported by a short-term Battery Energy Storage System (BESS) and limited, controlled interaction with the electrical grid.

Electrical energy is mainly provided by a photovoltaic (PV) plant and wind turbines (WTs). The installed capacities of the PV and WTs are design parameters that can be tuned to achieve the desired level of renewable penetration. The renewable electricity is used to directly supply the electrical demand of the ammonia production plant and to charge the storage systems, while possible surplus energy can be curtailed or exported to the grid. Due to the intrinsic variability of solar and wind resources, these generators alone cannot guarantee uninterrupted coverage of the plant demand, which motivates the inclusion of complementary storage technologies.

A BESS is introduced to provide short-term balancing and to improve the flexibility of the overall system. The BESS compensates for rapid fluctuations in PV and wind output and mitigates short-term mismatches between renewable generation and the ammonia plant demand. A dedicated PTES based on a Brayton cycle is adopted with a dual objective: it operates as a long-term energy storage system and is thermally coupled with the ammonia process to provide high-temperature heat. The thermal integration between the PTES and the ammonia plant is further enhanced by the recovery of process waste heat.

To guarantee the security of supply under all operating conditions, the system remains connected to the electrical grid. The grid can provide residual power when the combination of renewable generation, PTES discharging and BESS discharging is not sufficient to fully cover the ammonia plant electrical demand. Conversely, when there is surplus renewable electricity and the storage systems cannot absorb additional energy, power can be exported to the grid. In order to preserve the "green" character of the ammonia production, the contribution of grid electricity is limited by imposing a maximum admissible fraction of the annual electrical energy supplied by the grid relative to the total annual electrical energy consumption. This constraint effectively caps the share of non-renewable electricity and drives the sizing and operating conditions of the PV plant, wind farm, BESS and PTES subsystems.

To investigate the performance of the proposed system configuration, this study adopts a sequential three-step simulation and optimization approach, as shown in Fig. 2. First, a detailed model of an ammonia plant is developed in Aspen Plus. This first simulation model provides the electrical demand, thermal demand and recoverable waste-heat streams used as boundary conditions for the subsequent PTES design. On the basis of these boundary conditions, a customized PTES configuration is designed and simulated in EBSILON Professional. The results from the PTES model are then used to evaluate the thermodynamic performance of the storage system and to derive the performance parameters adopted in the optimization stage. In parallel, the expected hourly production profiles of the PV plant and wind farm are generated in MATLAB using the meteorological data of the selected site. Finally, a Mixed-Integer Linear Programming (MILP) problem is formulated in GAMS and solved using CPLEX to determine the optimal sizing of the overall renewable energy–PTES supply system required to satisfy the thermal and electrical demands of the ammonia production plant.

2.2. Green ammonia plant modelling

The green ammonia plant is modelled at an industrial scale with a production capacity of 100 tons/day, following the modelling approach proposed in Ref. [32]. Fig. 3 illustrates the block diagram of the Haber-Bosch synthesis process for ammonia production.

As shown, the nitrogen feed (N2FEED) and hydrogen produced by water electrolysis (H2FEED) are introduced into the ammonia plant in a 1:3 M ratio. These fresh feed streams are then combined with the recycled stream of unreacted gases to form the reactor inlet mixture. The resulting gas mixture, initially near ambient temperature, must be heated to the reactor operating temperature of 450°C. This heating is achieved in three steps: first, via heat exchange with the hot outlet stream from the reactor (HTX-1); second, through heat released by the exothermic ammonia synthesis reaction (HEAT-1); and finally, by

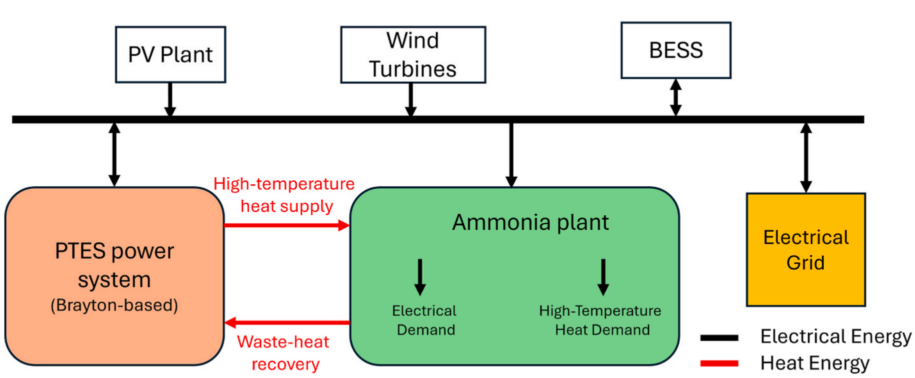

Fig. 1. Conceptual configuration of the RES-PTES supply system for an ammonia production plant.

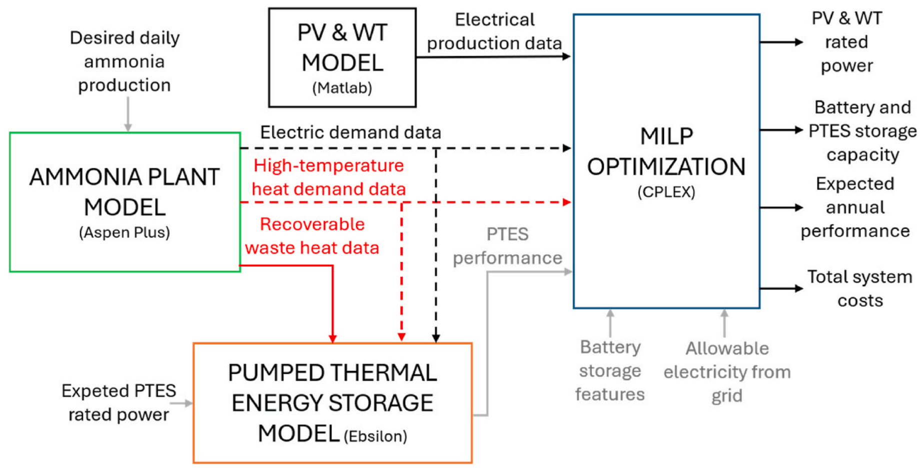

Fig. 2. Overall modelling and optimization workflow adopted in this study.

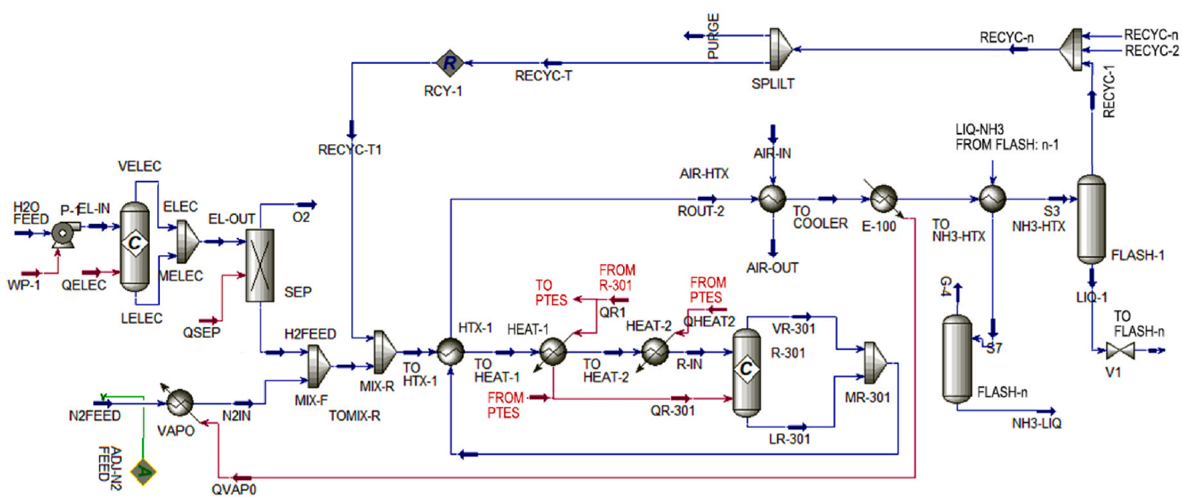

Fig. 3. Block diagram of the Haber-Bosch process for ammonia production.

supplemental thermal input from the PTES system (HEAT-2). Internal heat recovery from the exothermic ammonia synthesis reaction enables the feed mixture to reach approximately 430°C, but the remaining 20°C temperature increase required to reach the optimal reactor inlet condition must be provided by high-temperature thermal energy supplied by the PTES system.

The ammonia synthesis reaction occurs within a catalytic reactor at 180 bar and 450°C. The exothermic nature of the reaction releases significant thermal energy, almost 50% of which is reused internally for preheating the incoming gas mixture, while the surplus is recoverable and redirected to the PTES unit. Following the reaction, the product stream is cooled through a series of heat exchangers and pressure-reduction stages in order to condense the ammonia. The final condensation temperature reaches approximately −32°C. Separation is achieved in flash units, while unreacted gases are compressed in a multi-stage system for recycling.

The green ammonia production model was developed in Aspen Plus under steady-state conditions. The non-random two-liquid (NRTL) thermodynamic model was adopted for liquid-phase calculations, while the ideal gas model was used for gaseous streams. The ammonia synthesis reactor was represented as an isothermal multi-bed plug-flow reactor. A single-pass ammonia conversion of 20% was imposed, consistently with industrial operating conditions and literature-based kinetic correlations [32]. The reactor configuration consists of a catalytic multi-bed arrangement, with intermediate cooling between catalyst beds implicitly represented through the isothermal reactor assumption.

The main heat exchangers of the synthesis loop were modelled using rigorous counter-current HEATX blocks. In HTX-1, the hot synthesis gas leaving the reactor enters at approximately 450°C and is cooled to about 120°C, while preheating the reactor inlet stream. The heat exchangers involved in the thermal coupling with the PTES, namely HEAT-1 and HEAT-2, were also modelled as counter-current heat exchangers. For these units, an overall heat-transfer coefficient of 150 $W/m^2{\cdot}K$, a minimum temperature approach of 15°C, and pressure losses of 0.5 bar on each side were assumed. These assumptions are representative of industrial shell-and-tube heat exchangers designed for high-pressure hydrogen, nitrogen and ammonia-containing streams. After HTX-1, the process gas enters an air-cooling stage where its temperature is reduced from 120°C to approximately 40°C using ambient air as the cooling medium. This exchanger was modelled as a finned-tube air cooler with an estimated overall heat-transfer coefficient of 80 $W/m^2{\cdot}K$ and pressure losses of 0.2 bar. The final cooling stage before ammonia condensation was simulated as a refrigeration heat exchanger operating with a low-temperature refrigerant loop. In this unit, the gas stream is cooled from approximately 40°C to 0°C before entering the flash separation train, where further cooling associated with pressure reduction allows the final condensation temperature of approximately −32°C to be reached. The refrigeration exchanger was modelled with an assumed overall heat-transfer coefficient of 400 $W/m^2{\cdot}K$, with evaporation temperatures in the range from −10°C to 5°C. Ammonia- or propane-based refrigeration media were considered representative heat-transfer fluids for this cooling duty. The ammonia separation system consisted of four flash tanks operating sequentially at 180, 50, 10, and 1 bar. Intermediate cooling between pressure reduction stages promoted ammonia condensation and enhanced product purity. The vapor streams leaving the first three flash tanks, containing predominantly unreacted hydrogen and nitrogen, were recycled to the synthesis loop. The final liquid ammonia product stream contained less than 200 ppm of impurities.

2.3. Pumped thermal energy storage modelling

To supply the thermal and electrical demands of the green ammonia plant, a customized PTES system is developed using EBSILON Professional. The system operates on a closed-loop regenerative Brayton cycle, using air as the working fluid. It is designed to recover waste heat from the ammonia synthesis process, to supply high-temperature heat during operation, and to deliver electricity to the plant when needed, particularly during periods of low renewable energy availability. The PTES configuration comprises multi-stage compressors, turbines, heat exchangers and two thermal energy storage (TES) systems: a two-tank high-temperature TES filled with HITEC molten salts (operating up to 550°C) and a two-tank cold-TES using methanol as the storage medium. Fig. 4 shows the PTES system configuration proposed for the charging and discharging phases, respectively.

During the charging phase, the PTES system deviates from a conventional Brayton-based PTES configuration by incorporating two additional heat exchangers, NH_3HEX-1 and NH_3HEX-2, which enable thermal integration with the ammonia plant. After compression, the high-pressure air reaches its peak temperature. Rather than flowing directly to the thermal storage unit, the air first passes through NH_3HEX-2, where it releases heat to the ammonia plant. This thermal input supports the final stage of preheating of the reactor feed, helping to raise the mixture to the target inlet temperature of 450°C. Following this, the working fluid enters Salt-HEX, where its remaining high-grade thermal energy is transferred to the molten salt thermal energy storage (MS storage). The air then passes through the regenerator (REG) for internal heat recovery, reducing its temperature to below 40°C. To further cool the air and meet the requirements of the cold TES, a water cooler is introduced, bringing the temperature down to 30°C. After expansion through the turbine, the air is routed through MeOH-HEX, where cold thermal energy is transferred to the methanol storage. The cycle then proceeds with a first-stage temperature increase via the regenerator. Subsequently, the air passes through NH_3HEX-1, where it absorbs waste heat from the ammonia reactor, with steam assumed as the intermediate heat-transfer fluid. This recovered heat raises the inlet temperature of the compressor, which, at a fixed pressure ratio, increases the maximum temperature reached in the cycle. This thermal contribution improves the overall energy storage performance and enhances the coefficient of performance (COP) during the charging phase.

During the discharging phase, the PTES system operates to supply both high-temperature heat and electricity to the ammonia plant. The compressed air first enters the regenerator, where it absorbs heat from the turbine exhaust stream, initiating preheating. It then flows through NH_3HEX-1 to recover thermal energy from steam produced in the ammonia reactor. This external heat recovery reduces the thermal load on the molten salt storage, thereby preserving its thermal capacity and reducing the amount of stored energy required per cycle. The working fluid passes through Salt-HEX, where it receives high-grade heat from the molten salt storage. This raises the air temperature up to approximately 540°C, preparing it for energy conversion in the turbine. However, before entering the turbine, the air passes through NH_3HEX-2, where it releases part of its energy to preheat the feed mixture of the ammonia plant. After expanding through the turbine and generating electricity, the lower-pressure air continues through the regenerator, where it transfers heat to the incoming air stream. It is then cooled further, first in a water cooler and then through heat exchange with the methanol cold storage.

For each investigated PTES configuration, the rated electrical powers in charging and discharging modes are defined through the PTES-to-load fraction and the charging-to-discharging fraction introduced in Section 2.4. Accordingly, the mass flow rate of the working fluid, air, was adjusted to satisfy the prescribed power rating in each operating mode. The mass flow rates of the storage media (molten salts and methanol) were determined based on the targeted outlet temperatures of the working fluid at the respective heat exchangers. Specifically, the outlet temperature after Salt-HEX was set to 350°C during the charging phase and 540°C during the discharging phase while, for MeOH-HEX, the outlet temperature was fixed at 10°C during the charging phase and −15°C during the discharging phase. To maintain realistic and efficient thermal exchange, a minimum temperature difference of 10°C was imposed across all heat exchangers, except for the regenerator, for which the minimum temperature difference was increased to 30°C due to gas-to-gas heat exchange. In addition, a maximum air temperature of about 600°C at the compressor outlet was imposed. This limit reflects current material constraints and represents the upper threshold typically achieved by commercially available high-performance compressors. This maximum air temperature constitutes a key constraint during the optimization of the cycle, especially under the fixed pressure ratios adopted for charging and discharging. Table 2 reports the main technical specifications used for the PTES modelling.

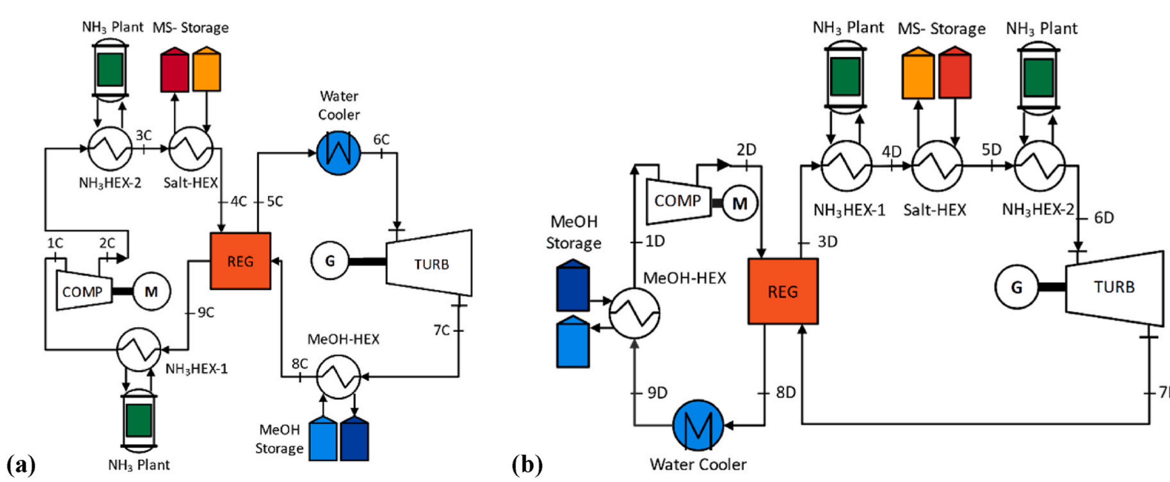

Fig. 4. Brayton-cycle pumped thermal energy storage system during: (a) charging and (b) discharging phases.

Table 2
Technical specifications of the PTES system.

Parameter	Value	Units
Turbine polytropic efficiency	0.90	-
Compressor polytropic efficiency	0.85	-
Minimum cycle pressure	1	bar
Compression Ratio (β)	2-5 (variable)	-
Relative Pressure Losses	0.02	
Water Cooler Inlet Temperature	20	°C
High-Temperature Storage Medium	HITEC Molten Salt	-
Cold storage medium	Methanol	-
Electromechanical Efficiency	0.97	-

In addition to the design-point simulations, the performance of the PTES system under part-load operating conditions was evaluated using the off-design calculation mode available in EBSILON Professional. A dedicated control system was implemented to impose the desired part-load operating point, expressed as a fraction of the nominal electrical power absorbed during the charging phase or produced during the discharging phase. The control action was performed by adjusting the mass flow rate of air circulating within the closed Brayton cycle, while maintaining the cycle configuration and the main operating constraints adopted at design conditions. The off-design behaviour of the turbomachinery was taken into account by introducing the variation of compressor and turbine isentropic efficiencies as functions of the working fluid mass flow rate relative to its nominal value. Moreover, the off-design behaviour of the heat exchangers was represented by allowing the heat transfer capability, expressed as the product of the overall heat-transfer coefficient and the heat-transfer area (UA), to vary with the operating mass flow rate. The characteristic curves adopted for compressors, expanders and heat exchangers under part-load operation are provided in the Supplementary Material.

To evaluate the effectiveness of the PTES system and support its optimization, two key performance indicators were defined: the total coefficient of performance (COP_T) for the charging phase and the thermal efficiency (η_{th}) for the discharging phase. In both cases, useful energy outputs also include the thermal energy delivered to meet the high-temperature heat demand of the ammonia plant. The COP_T is determined using Equation (1) as the ratio of the useful thermal energy stored, which includes the thermal energy transferred to the molten salt storage ($\dot{Q}_{MS,C}$) and to the methanol storage ($\dot{Q}_{MeOH,C}$), as well as the thermal energy supplied to the ammonia process ($\dot{Q}_{NH3}$), to the electrical energy consumed by the PTES system ($\dot{W}_{PTES,C}$).

$$COP_T = \frac{\dot{Q}_{MS,C} + \dot{Q}_{MeOH,C} + \dot{Q}_{NH3}}{\dot{W}_{PTES,C}} = \frac{\dot{m}_{MS}\left(h_{MS,o} - h_{MS,i}\right) + \dot{m}_{MeOH}\left(h_{MeOH,i} - h_{MeOH,o}\right) + \dot{Q}_{NH3}}{\dot{W}_{cmp,C} - \dot{W}_{tur,C}} \tag{1}$$

Together with the definition of the total COP_T as the main performance index of the PTES during the charging phase, two auxiliary sub-indicators are also introduced. The first one, COP_{MS}, is defined as the ratio between the thermal power stored in the molten salt tank ($\dot{Q}_{MS,C}$) and the electrical power absorbed by the PTES ($\dot{W}_{PTES,C}$). The second one, COP_{MeOH}, is defined analogously as the ratio between the thermal power stored in the methanol tank ($\dot{Q}_{MeOH,C}$) and the electrical power absorbed by the PTES. These two indicators, COP_{MS} and COP_{MeOH}, are later used in the optimization model to represent, in a compact form, the charging performance of the PTES hot and cold storage tanks, respectively.

The thermal efficiency (η_{th}) is calculated using Equation (2), as the ratio of the useful energy output during discharging, which includes electricity generation ($\dot{W}_{PTES,D}$) and process heat supply, to the thermal energy extracted from the two molten salt storage ($\dot{Q}_{MS,D}$) and the methanol storage ($\dot{Q}_{MeOH,D}$).

$$\eta_{th} = \frac{\dot{W}_{PTES,D} + \dot{Q}_{NH3}}{\dot{Q}_{MS,D} + \dot{Q}_{MeOH,D}} = \frac{\dot{W}_{tur,D} - \dot{W}_{cmp,D} + \dot{Q}_{NH3}}{\dot{m}_{MS}\left(h_{MS,i} - h_{MS,o}\right) + \dot{m}_{MeOH}\left(h_{MeOH,o} - h_{MeOH,i}\right)} \tag{2}$$

Similarly to the charging phase, two sub-indicators are introduced for the discharging phase. The first, $\eta_{th,MS}$, is defined as the ratio between the electrical power produced by the PTES during the discharging phase ($\dot{W}_{PTES,D}$) and the thermal power extracted from the molten salt tank ($\dot{Q}_{MS,D}$). The second, $\eta_{th,MeOH}$, is defined as the ratio between the electrical power produced by the PTES and the thermal power extracted from the methanol storage ($\dot{Q}_{MeOH,D}$). These two quantities, $\eta_{th,MS}$ and $\eta_{th,MeOH}$, are used in the optimization framework to characterize the effective conversion of stored hot and cold thermal energy into electricity during discharging.

In addition to the above indicators, the electrical round-trip performance of the PTES ($\eta_{\mathrm{PTES,RT}}$) is evaluated. Since the electrical power absorbed during charging and that produced during discharging may differ both from each other and from their nominal values, this indicator is defined on an annual energy basis as the ratio between the total electrical energy generated during the discharging phase and the total electrical energy absorbed during the charging phase:

$$\eta_{\mathrm{PTES,RT}} = \frac{\sum_t \dot{W}_{PTES,D}(t)}{\sum_t \dot{W}_{PTES,C}(t)} \tag{3}$$

This definition only accounts for the electricity recovered from the PTES and therefore differs from the combined thermo-electric indicators introduced above. To complement this indicator, an exergy-based round-trip efficiency ($\eta_{\mathrm{PTES,RTex}}$) is also introduced. In this case, the useful output includes both the electrical energy recovered during discharge and the exergy associated with the high-temperature process heat supplied to the ammonia plant ($\dot{Ex}_{\mathrm{NH_3}}$), while the input is the electrical energy absorbed during charging.

$$\eta_{\mathrm{PTES,RTex}} = \frac{\sum_t \left[\dot{W}_{PTES,D}(t) + \dot{Ex}_{\mathrm{NH_3}}\right]}{\sum_t \dot{W}_{PTES,C}(t)} \tag{4}$$

It is worth noting that the recovery of waste heat from the ammonia plant, through NH_3HEX-1, is regarded as an internal thermal interaction within the integrated system boundary. Consequently, it is not explicitly represented as an external input in the performance equations. However, its contribution is critical, as it reduces the net energy input required from external sources, thereby indirectly improving both the coefficient of performance and the thermal efficiency.

2.4. System design modelling

The optimal design of the proposed renewable energy–PTES supply system is formulated as a MILP problem aimed at minimizing the total system cost (TSC) while ensuring that the hourly electrical and thermal power demands of the reference ammonia plant, $\dot{W}_{NH3}$ and $\dot{Q}_{NH3}$, are satisfied over a full year with a time step of 1 h. The optimization is performed by imposing three main input parameters. The first one is the PTES-to-load fraction, $\phi_{\mathrm{PTES-L}}$, defined as the ratio between the nominal electrical power of the PTES during the discharging phase ($\dot{W}_{PTES,D,n}$) and the nominal electrical demand of the ammonia production plant. The second one is the PTES charging-to-discharging fraction, $\phi_{\mathrm{PTES,C-D}}$, defined as the ratio between the nominal electrical power in heat pump mode ($\dot{W}_{PTES,C,n}$) and the nominal electrical power in heat engine mode ($\dot{W}_{PTES,D,n}$). For a given pair $(\phi_{\mathrm{PTES-L}}, \phi_{\mathrm{PTES,C-D}})$, the nominal power ratings of the PTES sections are therefore obtained. The third input parameter of the optimization problem is the maximum percentage of electrical energy allowed from the grid, α_{GRID}. These three parameters are fixed a priori and define, respectively, the nominal power ratings of the PTES in both operating modes and the admissible contribution of grid electricity, while the remaining system components are optimally sized by the MILP.

Hourly production profiles for a single PV sub-array, $\dot{W}_{PV}$, and for a single wind turbine, $\dot{W}_{WT}$, are used as inputs to the optimization model. These profiles are generated following the methodology described by Marques da Cunha et al. [24] and are based on the meteorological conditions of a typical year for a coastal site in Morocco. The corresponding climate data (solar irradiance, ambient temperature, wind speed and air density) are taken from the Meteonorm database, which provides hourly time series representative of long-term averages. The PV sub-array is assumed to have a nominal electrical capacity of 1 MWp; its net power output is evaluated from the incident irradiance and ambient temperature by applying an overall efficiency factor that accounts for cell temperature, inverter losses and other minor losses. The wind turbine output is obtained from site-specific wind data at hub height, using the manufacturer's reference power curve and applying corrections for air density variations, wake effects and auxiliary consumptions, thus yielding an hourly time series of wind power production consistent with the selected Moroccan location. The main characteristics assumed for the PV sub-array and wind turbine models are reported in Table 3.

The objective function to be minimized represents the total system capital cost, including the investment cost of the renewable generators, the storage subsystems and the PTES unit. It is expressed as the sum of the specific cost c_i of each component i multiplied by its optimally determined size, plus the capital cost of the PTES section C_{PTES}. The decision variable set includes the integer numbers of PV sub-arrays and wind turbines, n_{PV} and n_{WT}, and the continuous capacities of the storage subsystems, namely the nominal storage capacity of the BESS $E_{B,n}$, the maximum thermal energy stored in the s storage $E_{MS,n}$, and in the methanol storage $E_{MeOH,n}$. The PTES power ratings in charging and discharging modes, $\dot{W}_{\mathrm{PTES,C,n}}$ and $\dot{W}_{\mathrm{PTES,D,n}}$, are fixed for each optimization case through the imposed design parameters; therefore, C_{PTES} does not introduce additional decision variables in the optimization problem, but it contributes to the comparison among different PTES design configurations. The objective function is therefore written as:

$$minTSC = (c_{PV} \cdot n_{PV}) + (c_{WT} \cdot n_{WT}) + (c_B \cdot E_{B,n}) + (c_{MS} \cdot E_{MS,n}) + (c_{MeOH} \cdot E_{MeOH,n}) + C_{PTES} \tag{5}$$

The optimization is subject to a set of constraints describing electrical balances, capacity limits and storage dynamics. Equation (6) represents the hourly electric power balance at the ammonia plant bus and imposes that PV and wind powers directly supplied to the plant load ($\dot{W}_{PV-NH3}$ and $\dot{W}_{WT-NH3}$ respectively), the power produced by the PTES during discharging phase and directly delivered to the load ($\dot{W}_{PTES-NH3}$), the power discharged from the BESS ($\dot{W}_{B-NH3}$) and the power imported from the grid ($\dot{W}_{GRID}$) are equal to the electrical power demand of the ammonia plant ($\dot{W}_{NH3}$).

$$\dot{W}_{PV-NH3}(t) + \dot{W}_{WT-NH3}(t) + \dot{W}_{PTES-NH3}(t) + \dot{W}_{B-NH3}(t) + \dot{W}_{GRID}(t) = \dot{W}_{NH3}(t) \tag{6}$$

Equations (7) and (8) define the overall power produced by PV and WT that can be directly used by the ammonia plant, used for charging the BESS ($\dot{W}_{PV-B}$ and $\dot{W}_{WT-B}$) or for charging the PTES system ($\dot{W}_{PV-PTES}$ and $\dot{W}_{PV-PTES}$). Any surplus renewable production can be curtailed or exported to the grid.

$$\dot{W}_{PV}(t) \cdot n_{PV} \geq \dot{W}_{PV-NH3}(t) + \dot{W}_{PV-B}(t) + \dot{W}_{PV-PTES}(t) \tag{7}$$

$$\dot{W}_{WT}(t) \cdot n_{WT} \geq \dot{W}_{WT-NH3}(t) + \dot{W}_{WT-B}(t) + \dot{W}_{WT-PTES}(t) \tag{8}$$

The operation of the PTES within the optimization model is represented through Equations 9–13. Specifically, Equations (9) and (10) define the power absorbed or produced by the PTES in the charging and discharging phases, respectively. Auxiliary binary variables, $Y_{PTES,C}$ and $Y_{PTES,D}$, indicate whether the PTES is operating in the charging or discharging phase, respectively, and enforce minimum and maximum operating powers. Equation (11) prevents simultaneous operation of the PTES in both modes. Equation (12) represents the evolution over time of the energy content in the MS storage (E_{MS}). This storage has a dual role in the proposed configuration. On the one hand, it acts as the hot thermal reservoir of the PTES and supplies thermal energy to the Brayton cycle during the discharging phase for electricity production. On the other hand, it acts as a thermal buffer for the ammonia plant, ensuring the supply of the required process heat. When the PTES is operating, either in charging or discharging mode, the process heat is provided through the thermal integration with the PTES cycle. Conversely, when the PTES is in idle mode, the process heat demand is directly covered by the MS storage. Finally, Equation (13) represents the evolution of the energy stored in the MeOH storage (E_{MeOH}) but, in this case, no external thermal load must be satisfied. Both E_{MS} and E_{MeOH} are bounded by the nominal storage capacities of the MS tanks ($E_{MS,n}$) and the methanol tanks ($E_{MeOH,n}$) respectively. It is worth noting that the performance coefficients adopted in the thermal storage balances are derived from the PTES performance maps obtained in EBSILON Professional. Since the electrical power absorbed or produced by the PTES varies at each time step according to renewable availability, storage state and plant demand, the corresponding performance coefficients (COP_{MS}, COP_{MeOH}, $\eta_{th,MS}$ and $\eta_{\mathrm{th,MeOH}}$) are not constant. Directly introducing these load-dependent coefficients into the thermal storage balances would result in nonlinear products between PTES electrical power and the corresponding performance coefficient. Therefore, to preserve the MILP formulation, the thermal powers exchanged with the molten salt and methanol storages are represented through piecewise-linear functions.

Table 3
Input parameters assumed for the modelling of the PV plant and wind farm.

Parameter	Value	Units
PV module		
PV module nominal power	250	Wp
PV nominal efficiency	0.1517	
Net operative cell temperature	47	°C
Temperature coefficient of power	−0.0045	1/°C
Wind turbine		
Wind turbine rated power	2	MW
Rotor diameter	110	m
Hub height	100	m
Cut-in wind speed	4	m/s
Cut-out wind speed	20	m/s
Rated wind speed	12	m/s

$$\dot{W}_{PTES,C,min}\cdot Y_{PTES,C}(t)\leq \dot{W}_{PTES,C}(t) = \dot{W}_{PV-PTES}(t)+\dot{W}_{WT-PTES}(t)+\dot{W}_{B-PTES}(t) \leq \dot{W}_{PTES,C,n}\cdot Y_{HP}(t) \quad (9)$$

$$\dot{W}_{PTES,D,min}\cdot Y_{PTES,D}(t)\leq \dot{W}_{PTES,D}(t)=\dot{W}_{PTES-NH3}(t)+\dot{W}_{PTES-B}(t)\,) \leq \dot{W}_{PTES,D,n}\cdot Y_{PTES,D}(t) \quad (10)$$

$$Y_{PTES,C}(t)+Y_{PTES,D}(t)\leq 1 \quad (11)$$

$$E_{MS}(t)=E_{MS}(t-1)+\left[\mathrm{COP}_{MS}(t)\cdot \dot{W}_{PTES,C}(t) - \frac{\dot{W}_{PTES,D}(t)}{\eta_{th,MS}(t)} - \dot{Q}_{NH3}(t)\cdot\left(1-Y_{PTES,C}(t)-Y_{PTES,D}(t)\right)\right]\cdot\Delta t\leq E_{MS,n} \quad (12)$$

$$E_{MeOH}(t)=E_{MeOH}(t-1)+\left[\mathrm{COP}_{MeOH}(t)\cdot \dot{W}_{PTES,C}(t)-\frac{\dot{W}_{PTES,D}(t)}{\eta_{th,MeOH}(t)}\right]\cdot\Delta t \leq E_{MeOH,n} \quad (13)$$

The state of charge of the BESS, E_B, evolves according to Equation (14), which includes the contributions of PV, wind and PTES in charging mode, multiplied by the charging efficiency $\eta_{B,C}$, and the discharging powers towards the ammonia plant and the PTES, penalized by the discharging efficiency $\eta_{B,D}$. The battery energy content is constrained not to exceed the design capacity $E_{B,n}$.

$$E_B(t)=E_B(t-1)+\left[\left[\left(\dot{W}_{PV-B}(t)+\dot{W}_{WT-B}(t)+\dot{W}_{PTES-B}(t)\right)\right]\cdot\eta_{B,C} - \frac{\dot{W}_{B-NH3}(t)+\dot{W}_{B-PTES}(t)}{\eta_{B,D}}\right]\cdot\Delta t\leq E_{B,n} \quad (14)$$

Finally, Equation (15) limits the total annual electrical energy imported from the grid to a prescribed fraction α_{grid} of the total annual electrical demand of the ammonia plant. This constraint ensures that the share of grid electricity, and thus of potentially non-renewable energy, remains below a threshold.

$$\sum_t \dot{W}_{GRID}(t)\leq \alpha_{GRID}\cdot\sum_t \dot{W}_{NH3}(t) \quad (15)$$

Table 4 reports the economic and technical input parameters adopted for solving the optimization problem.

To account for the investment cost of the PTES power block in the total system cost, the capital cost C_{PTES} was calculated by considering the main equipment of the Brayton cycle, namely compressors, turbines, electric motor/generator and heat exchangers (molten salt and methanol storage capacities are already included in the objective function):

$$C_{PTES}=C_{cmp,c}+C_{cmp,d}+C_{tur,c}+C_{tur,d}+C_{mot}+C_{gen}+\sum C_{HEX} \quad (16)$$

The adopted cost correlations, reported in Table 5, were taken from Ref. [33]. Costs were updated to the reference year 2024 using the Chemical Engineering Plant Cost Index (CEPCI), assumed equal to 800.

Finally, to quantify the benefit associated with the introduction of the proposed PTES-assisted supply configuration, an additional baseline configuration without PTES was considered. In this reference system, the electrical demand of the ammonia plant is supplied by the renewable generators, the grid and the BESS, which represents the only electrical energy storage subsystem. The thermal demand of the ammonia plant is supplied through the molten salt storage, which is also retained in the baseline configuration in order to decouple heat generation from the continuous process heat requirement. However, in the absence of the PTES, the molten salt storage is charged by an electric heater powered by the renewable generators, the BESS or the grid according to the adopted operating strategy. The baseline configuration is optimized using the same meteorological data, grid-energy constraint and economic assumptions adopted for the PTES-based system, and its total system cost is used as a reference for evaluating the economic advantage of the proposed PTES-assisted configuration.

Table 4
Input parameters assumed for the overall system design.

Parameter	Value	Units
PV sub-array capacity	1	MWp
PV sub-array specific cost (c_{PV})	800	$/kWp
Wind turbine specific cost (c_{WT})	1000	$/kW
BESS charging efficiency ($\eta_{B,C}$)	0.95	-
BESS discharging efficiency ($\eta_{B,D}$)	0.95	-
BESS specific cost (c_B)	280	$/kWh
Molten salt storage specific cost (c_{MS})	12.5	$/kWh
Methanol storage specific cost (c_{MeOH})	20	$/kWh

Table 5
Cost correlations adopted for the PTES section equipment.

Component	Cost correlation	Assumptions
Turbine	$C_{tur}=1.051\cdot\frac{266.3\cdot\dot{m}}{0.94-\eta_{is,T}}\beta\ln(\beta)$	
Compressor	$C_{cmp}=f_m\cdot 1.051\cdot\frac{39.5\cdot\dot{m}}{0.90-\eta_{is,C}}\beta\ln(\beta)$	$f_m=2$ for CMP used in charging phase; $f_m=1$ for CMP used in discharging phase
Electric motor	$C_{mot}=399400\left(\frac{\dot{W}_{cmp}}{1000}\right)^{0.61}$	
Electric generator	$C_{gen}=108900\left(\frac{\dot{W}_{tur}}{1000}\right)^{0.55}$	-
Heat exchangers	$C_{HEX,i}=49.45\left(\frac{\dot{Q}_i}{F_i\,LMTD_i}\right)^{0.75}$	$F_i=0.95$

Table 6
Main performance parameters of the ammonia production plant.

Parameter	Value	Units
Ammonia daily production	100	tons/day
Ammonia plant electric consumption ($\dot{W}_{NH3}$)	8	MW
Hydrogen generation consumption	37.5	MW
Total process heat demand ($\dot{Q}_{NH3}$)	1.2	MW
Waste heat available	2.7	MW
Low-grade waste heat (<100°C)	1.8	MW

3. Results and discussion

The performance of the ammonia production plant, simulated using Aspen Plus to quantify the thermal demand, electrical consumption and waste-heat recovery potential, is summarized in Table 6 (the main stream properties are reported in the Supplementary Material). As reported, the simulation predicts a total electrical demand of 45.5 MW, corresponding to a specific electricity consumption of 10,920 kWh/t_{NH3}. The predicted total electricity consumption is in close agreement with recent literature data. De la Hera et al. [34] reported 10,130 kWh/t_{NH3} for a flexible small-scale alkaline-based green ammonia plant, whereas Tully et al. [35] reported 10,500 kWh/t_{NH3} for an off-grid PEM-based system. The deviations of the present model are limited to 7.8% and 4.0%, respectively, which are within the uncertainty expected from differences in electrolyzer efficiency, operating pressure, compressor performance, pressure losses, heat integration, nitrogen production strategy and auxiliary loads. The majority of the plant's electrical demand (37.5 MW) is required for hydrogen production by water electrolysis. Consequently, electrolysis accounts for 82.4% of the total plant electricity demand, in agreement with the energy distributions reported in Refs. [34,35], confirming that hydrogen production is the dominant energy-consuming unit. However, due to the flexibility of electrolyzers and the feasibility of hydrogen storage, this part of the system can be directly supplied by PV and WT systems. In contrast, the Haber-Bosch ammonia synthesis loop must operate continuously, with a stable electricity supply ($\dot{W}_{NH3}$) of approximately 8 MW to maintain process reliability. Therefore, the proposed PTES-assisted renewable energy supply configuration is designed to cover this constant power requirement, acting as a buffer against renewable intermittency. In addition to electrical support, the PTES system is required to deliver $\dot{Q}_{NH3} =$ 1.2 MW of thermal energy to heat a feed gas mixture (approximately 5.3 kg/s) from 430°C to 450°C, covering the shortfall in internal heat recovery within the ammonia synthesis loop. Regarding waste heat recovery, the plant produces roughly 2.7 MW of recoverable high-temperature waste heat, primarily from the reactor and downstream separation units. This energy is suitable for recovery and reuse within the PTES cycle. Conversely, about 1.8 MW of waste heat is classified as low-grade heat, below 100°C, and does not provide a significant thermodynamic benefit when recovered by the PTES system.

3.1. Performance analysis of the pumped thermal energy storage

Based on the outputs of the reference ammonia plant simulation, a parametric analysis was carried out to evaluate the influence of the compression ratio β on the PTES performance during both the charging and discharging phases. The aim was to identify, for different PTES sizes, the operating conditions that maximize the performance indicators of the system, namely the total coefficient of performance of the PTES during the charging phase and the thermal efficiency η_{th} of the PTES system during the discharging phase. Fig. 5(a) reports the variation of the overall thermal efficiency η_{th} during the discharging phase as a function of the compression ratio for different values of the PTES-to-load fraction ϕ_{PTES-L}. For all configurations, the efficiency initially increases with the compression ratio β. This trend is associated with the thermal interaction between the PTES cycle and the waste-heat streams available from the ammonia plant: as β rises, the temperature of the working fluid at the turbine outlet decreases, reducing the heat exchanged in the internal recuperator and increasing the fraction of the available waste heat from the ammonia process that can be usefully recovered to preheat the PTES working fluid. As a consequence, the thermal energy required from the molten salt storage decreases. The efficiency reaches a maximum when the PTES is able to fully exploit the available high-temperature waste heat from the ammonia plant. Beyond this point, a further increase in the compression ratio causes a reduction in η_{th}, as expected for a regenerative Brayton cycle, due to the growing irreversibility and the larger compressor work required. The impact of waste heat recovery becomes more pronounced when the PTES discharging power rating is reduced, that is, for lower values of ϕ_{PTES-L}. In this case, the same amount of recoverable heat is distributed over a smaller electrical output, leading to higher values of η_{th} and to optimal operation at lower compression ratios. Fig. 5(b) shows the trend of the total coefficient of performance in charging mode, COP_T, as a function of the compression ratio for different values of the charging-to-discharging fraction, $\phi_{PTES,C-D}$, with ϕ_{PTES-L} fixed at 0.5. Similar behaviours are observed for the other values of ϕ_{PTES-L}. The minimum admissible compression ratio depends on $\phi_{PTES,C-D}$ and is dictated by the requirement to heat the molten salt up to 550°C. For small charging power ratings, corresponding to low values of $\phi_{PTES,C-D}$, the recovery of heat released by the ammonia plant has a particularly significant influence, leading to a marked increase in the working fluid temperature before compression. Under these conditions, the maximum compressor-outlet temperature constraint limits the feasible pressure-ratio range and the amount of waste heat that can be effectively recovered. As $\phi_{PTES,C-D}$ increases, the cycle can accommodate a larger fraction of recovered heat while respecting the maximum temperature constraint, and COP_T reaches its maximum. When $\phi_{PTES,C-D}$ is further increased, the maximum value of COP_T decreases. This behaviour is due to the reduced relative contribution of both the heat delivered to the ammonia plant and the heat recovered from it, while the electrical power absorbed in heat pump mode increases with the larger PTES charging power rating.

On the basis of these results, for each combination of ϕ_{PTES-L} and $\phi_{PTES,C-D}$ the pressure ratio that maximizes the total coefficient of performance COP_T in charging mode and the thermal efficiency η_{th} in discharging mode was selected as the design point of the PTES. The corresponding PTES cycles at the selected optimal design points, including the main stream properties, are reported in the Supplementary Material. Starting from these PTES configurations, an off-design analysis was carried out to assess the effect of part-load operation on the performance parameters adopted in the optimization model. Fig. 6 shows the variation of the charging performance indicators, COP_{MS} and COP_{MeOH}, and of the discharging performance indicators, η_{MS} and η_{MeOH}, as functions of the PTES load fraction.

The admissible part-load range differs significantly between the two operating modes. During charging, the minimum achievable operating load is approximately 70% of the nominal absorbed power, whereas

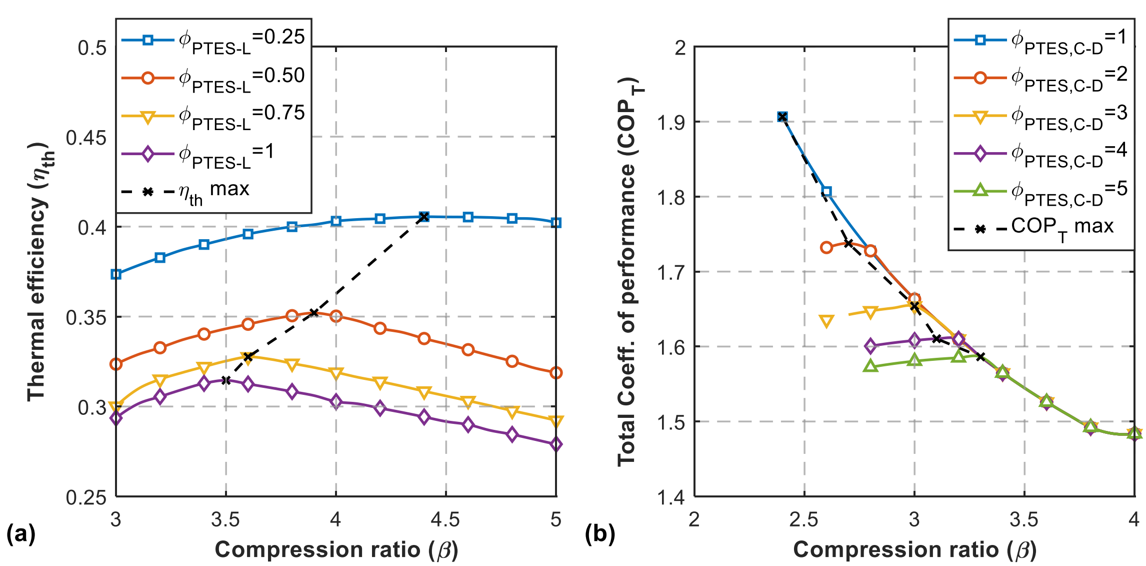

Fig. 5. Thermodynamic performance analysis of the PTES system as a function of compression ratio: (a) thermal efficiency during discharging for different PTES-to-load fractions; (b) total coefficient of performance during charging for different charging-to-discharging fractions.

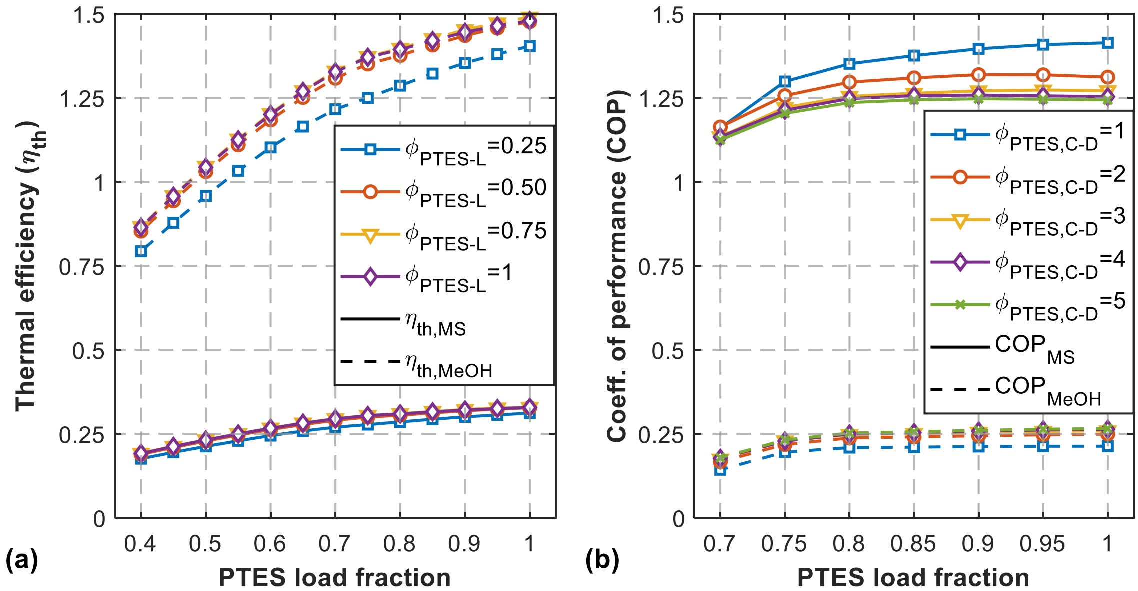

Fig. 6. Off-design performance of the PTES configuration selected at the design point: (a) variation of the discharging indicators η_{MS} and η_{MeOH} and (b) of the charging indicators COP_{MS} as functions of the PTES load fraction.

during discharging the PTES can operate down to approximately 40% of its nominal generated power. This result indicates a greater operational flexibility of the system in discharging mode. The more limited operating range during charging is mainly caused by the faster reduction in the working fluid mass flow rate required to decrease the absorbed electrical power. This behavior produces a more pronounced deterioration in turbomachinery efficiency and limits stable and thermodynamically effective operation at low charging loads. As an example of the off-design operating conditions, the stream properties of the PTES charging and discharging cycles at the minimum admissible load are reported in the Supplementary Material. As shown in Fig. 6, the charging indicators COP_{MS} and COP_{MeOH} remain nearly constant as the PTES load decreases from the nominal condition to approximately 80% of the rated charging power. Below this threshold, both indicators exhibit a more evident reduction, associated with the degradation of turbomachinery and heat-transfer performance under more severe part-load conditions.

During discharging, the indicators $\eta_{th,MS}$ and $\eta_{th,MeOH}$ decrease more progressively over the investigated operating range, reflecting the continuous effect of reduced mass flow rate and off-design machine efficiency on the conversion of stored thermal energy into electricity.

These results confirm that assuming constant design-point performance coefficients would not adequately represent the actual operation of the PTES, particularly in a system driven by variable renewable generation. Therefore, the off-design performance curves reported in Fig. 6 are used as inputs to the optimal sizing model through the piecewise-linear formulation described above, allowing the effects of PTES part-load operation on the molten salt and methanol storage balances to be taken into account.

3.2. Optimal system configuration

To analyze the influence of the PTES design parameters and of the

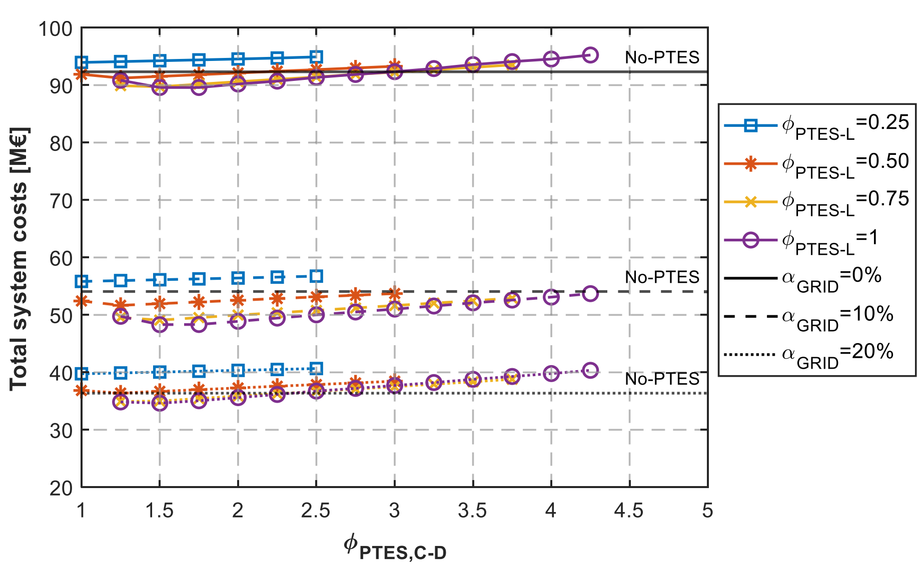

Fig. 7. Total system cost as a function of the PTES Charging-to-Discharging fraction ($\phi_{PTES,C-D}$) for several PTES-to-load fractions (ϕ_{PTES-L}) and the maximum grid share (α_{GRID}) values.

allowed grid contribution on the optimal renewable energy–PTES supply configuration, the results of the sizing optimization are presented. Fig. 7 shows the trend of the objective function, i.e. the total system cost (TSC), as a function of the charging-to-discharging fraction $\phi_{PTES,C-D}$ for different values of the PTES-to-load fraction ϕ_{PTES-L} (from 0.25 to 1.0 with a step of 0.25) and for three values of the maximum grid share α_{grid}. Solid lines refer to the fully renewable case (α_{GRID} = 0%), dashed lines to α_{GRID} = 10% and dotted lines to α_{GRID} = 20%. In general, the influence of $\phi_{PTES,C-D}$ and ϕ_{PTES-L} on TSC is relatively modest when compared with the impact of α_{GRID}. Allowing a limited contribution from the electrical grid, especially during periods of low renewable generation, leads to a substantial reduction in the required PV and WT capacities and storage capacities, and to a more effective use of the PTES system. As a consequence, accepting that 10% of the annual electrical energy demand is supplied by the grid reduces the TSC by almost 50% with respect to the fully renewable configuration. Increasing α_{GRID} to 20% yields an even lower TSC, with a reduction of about 65% compared to the case in which α_{GRID} = 0%; however, the marginal benefit of further relaxing the grid constraint becomes less pronounced.

For a given value of α_{GRID}, the choice of ϕ_{PTES-L} still plays a role. Regardless of the grid share, the configuration with a PTES power rating during the discharging phase equal to the maximum plant load ($\phi_{PTES-L} = 1$) generally provides the lowest TSC. In this case, the PTES can, in principle, fully cover the instantaneous electrical demand of the ammonia plant during discharging, without the need for concurrent support from renewable generators or the BESS. When α_{GRID} increases, configurations with slightly lower PTES-to-load fractions (i.e. ϕ_{PTES-L} = 0.75) become nearly cost-equivalent, since part of the residual demand can be economically met by the grid and the benefit of a large PTES power rating diminishes compared to the increased investment costs.

The dependence of TSC on $\phi_{PTES,C-D}$ reflects a trade-off between the increased investment cost of the PTES and the operational benefit associated with a larger charging capacity. For the investigated configurations, the minimum TSC is generally achieved for $\phi_{PTES,C\text{-}D}$ values of approximately 1.5. Increasing the PTES charging power rating allows a larger fraction of the surplus electricity generated by the oversized PV and WT to be converted into stored thermal energy, thereby reducing renewable overproduction that would otherwise be curtailed or exported. However, this benefit is progressively offset by the increased capital cost of the PTES equipment. Consequently, further increases in $\phi_{PTES,C\text{-}D}$ do not result in economically advantageous configurations. Part-load performance further affects this trend. A strong oversizing of the PTES charging power rating compared with the discharging rating not only leads to higher capital costs, but may also result in infeasible system configurations. In fact, the PTES can operate in charging mode only above approximately 70% of its nominal charging power. Therefore, when the charging section is excessively oversized, the minimum admissible charging power becomes too high compared with the surplus renewable power available during a significant number of hours. Under these conditions, the PTES cannot be effectively charged with the available renewable overproduction and may not accumulate sufficient thermal energy to satisfy the continuous heat demand of the ammonia plant. Fig. 7 also shows the TSC obtained for the reference configurations without PTES. Since these systems do not include the PTES power block, their cost is independent of $\phi_{PTES\text{-}L}$ and $\phi_{PTES,C\text{-}D}$, and the corresponding values are therefore represented as horizontal black lines for each value of α_{GRID}. Compared with these reference systems, the proposed PTES-assisted configuration achieves a reduction in TSC ranging from approximately 3% to 10%, depending on the allowed grid-energy contribution and the selected PTES sizing parameters. The advantage of the PTES-assisted configuration is particularly evident when a limited grid contribution is allowed, namely for α_{GRID} = 10%. Under these conditions, the grid reduces the need for extreme oversizing of renewable generation and storage, while the PTES can be operated more effectively within its admissible part-load range, resulting in the largest cost reductions with respect to the baseline configuration.

To further characterize the impact of the grid contribution on the optimal configuration, Fig. 8 summarizes the variation of the main design parameters as a function of α_{GRID}. Since the optimal sizes depend on the PTES power ratings, which are defined through $\phi_{PTES,C-D}$ and ϕ_{PTES-L}, the results are reported in the form of boxplots, representing the distribution of optimal values over the different PTES design combinations. Fig. 8(a) shows the variation of the installed power ratings of the two RES subsystems (PV and WTs), whereas Fig. 8(b) illustrates the corresponding variation of the storage capacities, namely the BESS, the molten salt storage and the methanol storage.

As can be observed from Fig. 8(a), increasing α_{GRID} leads to a clear reduction of the overall installed RES capacity, as expected, and also to a marked change in the relative contribution of the two technologies. In the fully renewable case (α_{GRID} = 0%), the PV plant is predominant: its optimal installed capacity is, on average, about five times higher than that of the wind farm. When the grid share is increased to 20%, the situation is reversed and the wind capacity becomes, on average, approximately 25% higher than the PV capacity. This behaviour is mainly related to the concomitant reduction of the storage capacities. Photovoltaic production follows a relatively regular diurnal pattern but

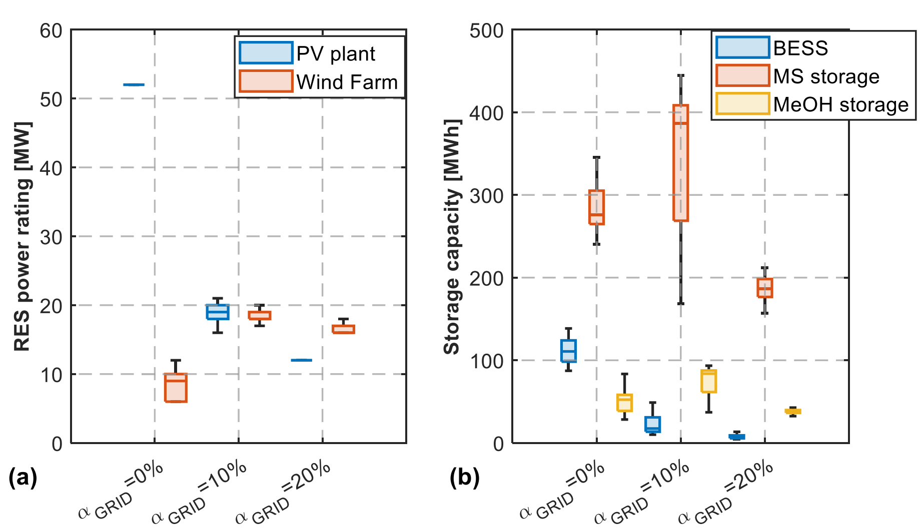

Fig. 8. Effect of the allowed grid share α_{GRID} on the optimal system design: (a) installed capacities of PV plant and wind farm; (b) storage capacities of the BESS, molten salt storage and methanol storage.

requires substantial storage to guarantee supply during night hours. Allowing part of the load to be covered by the grid, especially during periods of very low renewable production, relaxes the storage requirement and favors the exploitation of wind power, which is characterized by higher capacity factors and less pronounced daily seasonality at the selected site.

The effect of α_{GRID} on the storage subsystems is highlighted in Fig. 8 (b). The BESS exhibits a progressive decrease in its median optimal capacity as the admissible grid share increases, together with a narrowing of the corresponding boxplots. This trend is consistent with the reduction in the overall installed renewable generation capacity: as a larger fraction of the electrical demand can be supplied by the grid, the need for short-term electrical storage to compensate for fluctuations in PV and WT electricity production is reduced. A different trend is observed for the thermal storage capacities associated with the PTES. Both the molten salt and methanol storages show their highest median capacities, as well as the widest range of optimal values, for $\alpha_{\mathrm{GRID}} = 10\%$, followed by a decrease when the admissible grid contribution is further increased to 20%. This behaviour results from the role assumed by the PTES when a limited grid contribution is introduced. At $\alpha_{\mathrm{GRID}} = 10\%$, a substantial reduction in the installed PV and WT capacities is already observed compared with the fully renewable case; however, grid support is still sufficiently constrained that the PTES remains essential for medium- and long-duration energy management. Consequently, larger thermal storage capacities may be required to ensure adequate energy shifting under reduced renewable-generation oversizing. The larger dispersion of the molten salt and methanol storage capacities at $\alpha_{\mathrm{GRID}} = 10\%$ also indicates a stronger dependence of the optimal configuration on the PTES sizing parameters, particularly on $\phi_{\mathrm{PTES-L}}$. This behaviour is consistent with the total system cost trends reported in Fig. 7, where the influence of the PTES power rating becomes more evident for configurations with limited grid support. When α_{GRID} is increased to 20%, the greater flexibility provided by the grid reduces the need for both electrical and thermal storage, leading to a decrease in the optimal capacities of all storage subsystems.

On the basis of the previous results, and by allowing the grid to supply 10% of the annual electrical demand ($\alpha_{\mathrm{GRID}} = 10\%$), a reference optimal configuration of the PTES-assisted renewable energy supply system can be identified. Under this constraint, the PTES design that minimizes the total system cost corresponds to a PTES-to-load fraction $\phi_{\mathrm{PTES-L}} = 1$, i.e. a PTES power rating in discharging mode equal to the nominal electrical demand of the ammonia plant, and to a charging-to-discharging fraction $\phi_{\mathrm{PTES,C-D}} = 1.5$. For the considered case study, this implies a PTES electrical power rating of approximately 8 MW in discharging mode and 12 MW in charging mode. This configuration represents a satisfactory compromise between the exploitation of renewable resources, the utilization of the PTES unit and the economic benefit associated with a limited use of grid electricity, and is therefore adopted as the reference design for the subsequent analysis. Table 7 reports the thermodynamic performance metrics of the PTES system under these optimized conditions, while Fig. 9 shows the corresponding thermodynamic cycles in the temperature–entropy (T–s) diagram under nominal conditions.

The difference in the enclosed area between the charging and discharging cycles is directly proportional to the nominal round-trip efficiency of the system. The larger area under the discharging curve relative to the charging loop reflects the effective energy recovery achieved, corresponding to a nominal round-trip efficiency of approximately 41.9%. However, the requirement for continuous operations under part-load conditions reduces the round-trip efficiency to about 26%. A notable asymmetry in the maximum temperatures is observed: approximately 600°C during charging versus 540°C during discharging. This difference results from two main factors: (i) in the charging phase, the working fluid transfers heat to the ammonia plant via NH_3HEX-2 before reaching the Salt-HEX, requiring a higher compressor outlet temperature to meet both storage and process demands; (ii) in the discharging phase, the fluid must absorb thermal energy from Salt-HEX across a minimum temperature difference constraint ($\Delta T_{min} = 10$°C), which limits the maximum achievable temperature at the turbine inlet and constrains the efficiency of thermal recovery. A significant difference in minimum cycle temperatures also occurs: about −42.1°C in

Table 7
Thermodynamic performance metrics of the optimized PTES configuration.

Category	Parameter	Charging Phase	Discharging Phase	Units
Cycle Parameters	Compression Ratios (β)	3	3.5	–
	Air Mass Flow Rate	58.1	107.6	kg/s
Storage Media	Molten Salt Mass Flow Rate	48.0	74.2	kg/s
	Methanol Mass Flow Rate	27.8	50.2	kg/s
	MS storage capacity ($E_{MS,n}$)	426		MWh
	MeOH storage capacity ($E_{MeOH,n}$)	88		MWh
Heat Transfer	NH_3HEX-2 Heat Transfer ($\dot{Q}_{NH3}$)	1.2	1.2	MW
	Salt-HEX Heat Transfer ($\dot{Q}_{MS}$)	15.7	24.3	MW
	REG Heat Transfer	18.0	20.4	MW
	Water Cooler Heat Transfer	0.7	12.1	MW
	MeOH-HEX Heat Transfer ($\dot{Q}_{MeOH}$)	3.0	5.4	MW
	NH_3HEX-1 Heat Transfer	2.7	2.7	MW
Power Metrics	Compressor Power ($\dot{W}_{cmp}$)	16.8	14.1	MW
	Turbine Power ($\dot{W}_{tur}$)	4.8	22.1	MW
Performance Indices	Total Coefficient of Performance (COP_T)	1.654	–	–
	Thermal Efficiency (η_{th})	–	30.6%	–
	Annual round-trip efficiency ($\eta_{\mathrm{PTES,RT}}$)	0.26		
	Nominal round-trip efficiency	0.419		
	Exergy-based round-trip efficiency ($\eta_{\mathrm{PTES,RTex}}$)	0.44		

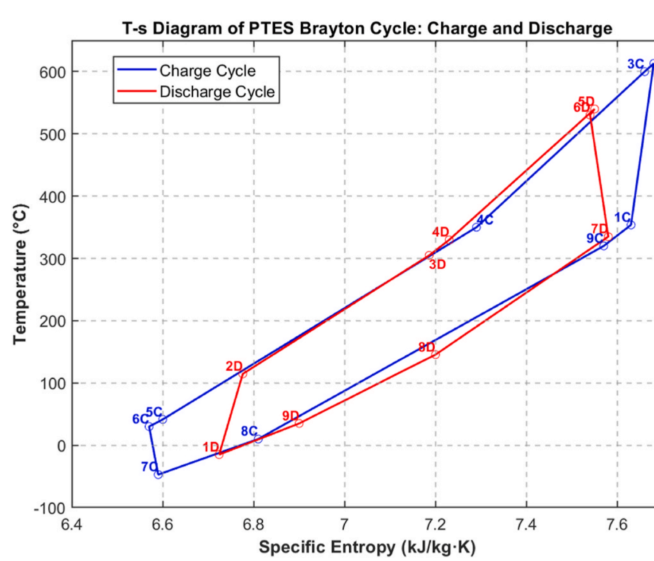

Fig. 9. Temperature–entropy diagrams of the optimized PTES configuration under nominal operating conditions.

charging versus −15°C in discharging. This variation originates from the minimum temperature difference constraint in MeOH-HEX, which limits the depth of cold thermal energy storage and recovery. While reducing this temperature gap could improve cold-side performance, it would require significantly larger heat exchanger surfaces, leading to increased capital costs and potential design complexity. In addition, the temperature of the air entering the water cooler differs substantially between the two cycles, approximately 41.4°C during charging and 145.7°C during discharging. These relatively low-grade heat levels demonstrate that recovering additional low-temperature waste heat from the ammonia plant (e.g., below 100°C) offers limited thermodynamic benefit and would not materially improve the performance of the PTES system, confirming the decision to exclude low-quality heat from the integration scope. Finally, the *T-s* diagram clarifies the role of the waste heat recovered from the ammonia synthesis process. This heat is effectively exploited as a preheating contribution; however, because of the high air mass flow rates in the PTES cycle, it increases the working fluid temperature by about 50°C. To further investigate the thermodynamic effect of this waste-heat recovery from the ammonia plant, a component-level exergy destruction analysis was performed for the optimized PTES configuration. The reference cycle with waste-heat recovery was compared with an alternative PTES configuration in which the contribution of the recoverable waste heat from the ammonia synthesis loop is not exploited. In this second case, the compression ratios maximizing the PTES performance indicators were recalculated, leading to only moderate variations in the optimal values: $\beta = 3.9$ during the charging phase and $\beta = 3$ during the discharging phase. The corresponding component-level exergy destruction rates are reported in Fig. 10. As shown, the variation of the compression ratio in the configuration without waste-heat recovery modifies the distribution of exergy destruction rates within the cycle. For the charging phase, the increase of the optimal β for the case without WHR results in an increase in exergy destruction in the compressor, regenerator and water cooler and a decrease in the turbine and MeOH-HEX. A reverse trend is observed during the discharging phase since the optimal β for the case without WHR is reduced. However, in both phases, if the exergy associated with the unrecovered waste-heat stream, reported as NH_3HEX-1* in Fig. 10, is not considered as part of the internal component irreversibilities, the total exergy destruction of the two configurations is almost comparable. This result indicates that the main thermodynamic advantage of the proposed configuration is not a strong reduction in the internal irreversibilities of the Brayton cycle itself, but rather the possibility of exploiting an otherwise unused high-temperature waste-heat stream from the ammonia plant. Therefore, the component-level exergy analysis confirms that waste-heat recovery is the key element enabling the PTES cycle to improve its overall exergy performance within the proposed renewable energy–PTES–ammonia system. Finally, to provide a subsystem-level benchmark of the PTES model, the performance indicators and main stream conditions of the optimized PTES configuration are compared in the Supplementary Material with those of a reference recuperated Brayton-cycle PTES system reported in the literature.

4. Conclusions

This study proposed a tailored PTES-assisted renewable energy supply configuration for a green ammonia production plant with a daily ammonia production of 100 tons, aiming to address the challenges posed by the intermittent nature of hybrid PV–wind generation and the continuous operation requirements of the Haber-Bosch process.

The thermodynamic analysis confirms the technical feasibility of the proposed PTES configuration. The recovered heat from the ammonia plant contributes to preheating the working fluid and improves the performance of the storage cycle.

The results showed that the allowed share of grid electricity has a dominant impact on the total system cost and on the optimal configuration, with cost reductions of approximately 50% and 65% when grid electricity is allowed to cover 10% and 20% of the annual electrical demand, respectively, compared with the fully renewable case. Regardless of the allowed grid contribution, a PTES power rating in discharging mode equal to the nominal electrical demand of the ammonia plant, combined with a charging power rating approximately 50% higher than the discharging rating, generally represents the optimal sizing. This configuration provides the most favorable compromise among the capability to absorb surplus renewable electricity, the ability to satisfy the energy requirements of the ammonia plant, the part-load operating limits and the investment cost of the PTES. The comparison with a reference configuration without PTES confirms the benefit of the proposed PTES-assisted configuration. Depending on the allowed grid contribution and on the selected PTES sizing parameters, the PTES-

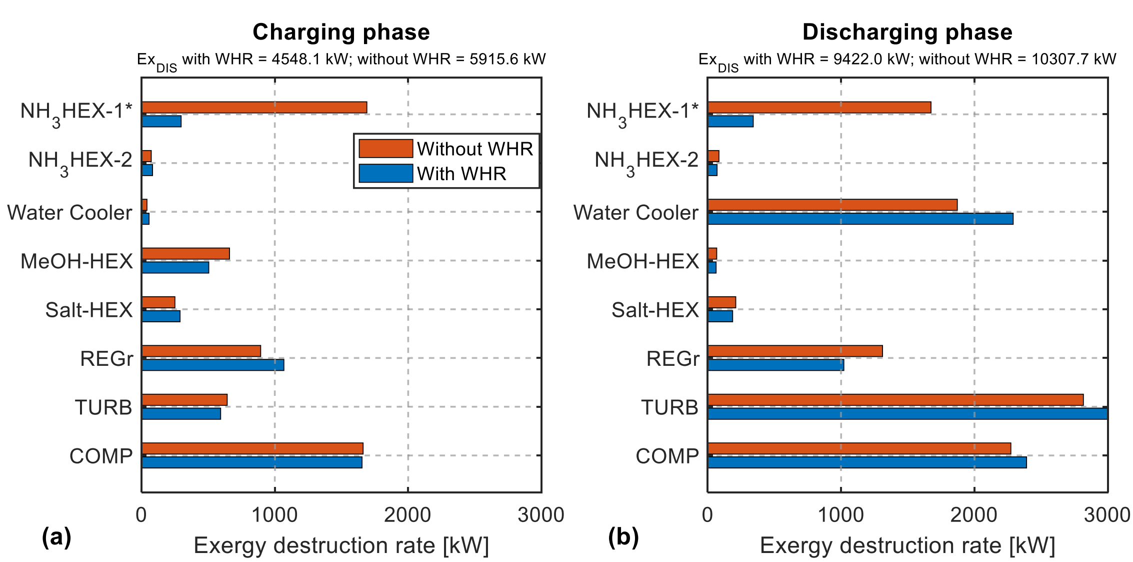

Fig. 10. Component-level exergy destruction of the optimized PTES configuration with and without waste-heat recovery from the ammonia plant under nominal operating conditions: (a) charging phase; (b) discharging phase. The asterisk on NH_3HEX-1 indicates that, in the case without WHR, the reported value corresponds to the exergy content of the recoverable waste-heat stream that is not exploited by the PTES and is therefore treated as lost exergy.

based configuration reduces the total system cost by approximately 3–10% compared with the reference case.

From an engineering perspective, the results therefore indicate that a tailored Brayton-cycle PTES system can represent a suitable long-duration storage option for renewable-powered ammonia plants requiring continuous electricity and high-temperature heat supply. In particular, the proposed architecture is advantageous when waste heat from the synthesis loop can be exploited within the storage cycle and when limited grid support is available to avoid extreme renewable and storage oversizing.

A limitation of the present study is that the ammonia plant is treated as a reference industrial process with fixed electrical and thermal demands, as well as recoverable waste-heat streams with given temperatures and mass flow rates. As a consequence, the PTES configuration is designed and optimized under constrained heat-source and heat-sink conditions, which can limit its performance. Future work may extend this approach by investigating whether modifications to the ammonia plant configuration or to the process heat-integration network could improve the overall performance of the renewable energy–PTES–ammonia system. In such a framework, local reductions in the stand-alone performance of the ammonia synthesis loop could be acceptable if they enable better waste-heat recovery, more effective PTES operation and a reduction in total system cost.

CRediT authorship contribution statement

Mostafa EsmaeiliShayan: Writing – original draft, Investigation, Formal analysis, Data curation, Conceptualization. **Giovanni Cirina:** Writing – original draft, Software, Methodology. **Mouad Arrad:** Writing – original draft, Software, Methodology, Investigation. **Ammar Mouaky:** Writing – review & editing, Validation, Formal analysis. **Mario Petrollese:** Writing – review & editing, Visualization, Supervision, Conceptualization.

Declaration of competing interest

The authors declare the following financial interests/personal relationships which may be considered as potential competing interests: Mostafa EsmaeiliShayan, Giovanni Cirina, Mouad Arrad, Ammar Mouaky and Mario Petrollese reports financial support was provided by European Union's Horizon 2020 Research and Innovation Program. If there are other authors, they declare that they have no known competing financial interests or personal relationships that could have appeared to influence the work reported in this paper.

Acknowledgment

This work was supported by the project “REPTES - Renewable Plants Integrated with Pumped Thermal Energy Storage for Sustainable Satisfaction of Energy and Agricultural Needs of African Communities” under the LEAP-RE programme. The LEAP-RE programme has received funding from the European Union's Horizon 2020 Research and Innovation Program under Grant Agreement No. 963530. The authors gratefully acknowledge this financial support, which has been instrumental in conducting this research.

Appendix A. Supplementary data

Supplementary data to this article can be found online at https://doi.org/10.1016/j.energy.2026.142171.

Nomenclature. Abbreviations

Term	Description	Term	Description
BESS	Battery Energy Storage System	*REG*	Regenerator/Recuperator
COP	Coefficient of Performance	*RES*	Renewable Energy Sources/Systems
HEX	Heat Exchanger	*SDG*	Sustainable Development Goals
LMTD	Logarithmic mean temperature difference	*TES*	Thermal Energy Storage
MILP	Mixed-Integer Linear Programming	*TI-PTES*	Thermally Integrated Pumped Thermal Energy Storage
MS	Molten Salt	*TSC*	Total System Cost
PTES	Pumped Thermal Energy Storage	*WHR*	Waste heat recovery
PV	Photovoltaic	*WT*	Wind Turbine

Symbols

Symbol	Unit	Description	Symbol	Unit	Description
c	\$/unit	Specific cost coefficient (per kW, kWp, or kWh)	T	°C, K	Temperature
E	kWh, MWh	Energy capacity or stored energy level	$\dot{W}$	kW, MW	Electrical power or mechanical work rate
$\dot{Ex}$	kW, MW	Exergy content	Y	{0,1}	Binary decision variable for operating mode
h	kJ/kg	Specific enthalpy	α_{grid}	–	Maximum allowable fraction of grid electricity contribution
$\dot{m}$	kg/s	Mass flow rate	β	–	Pressure ratio
n	–	Number of installed units	Δh	kJ/mol	Enthalpy change of reaction
P	bar	Pressure	η	–	Efficiency
$\dot{Q}$	kW, MW	Heat transfer rate (thermal power)	Φ_{PTES-L}	–	PTES-to-Load fraction (ratio of PTES discharge power to load)
t	h	Time step index	$\Phi_{PTES,C-D}$	–	PTES Charging-to-Discharging power ratio

Subscripts and Superscripts

Symbol	Description	Symbol	Description
B	Battery/BESS related	*MS*	Molten Salt storage
C	Charging phase	*n*	Nominal/Rated value
cmp	Compressor	*NH3*	Ammonia synthesis plant/process
D	Discharging phase	*o*	Outlet condition
grid	Electrical grid	*PV*	Photovoltaic system
i	Inlet condition	*th*	Thermal (efficiency)
MeOH	Methanol storage	*tur*	Turbine
min	Minimum limit	*WT*	Wind Turbine system

Data availability

Data will be made available on request.

References

[1] Pagani G, Hajimolana Y, Acar C. Green hydrogen for ammonia production – a case for the Netherlands. Int J Hydrogen Energy 2024;52:418–32. https://doi.org/10.1016/J.IJHYDENE.2023.06.309.

[2] Abdellatief TMM, Alami AH, Abdelkareem MA, Olabi AG. Environmental impact of green ammonia production. Reference Module in Materials Science and Materials Engineering 2025:511–22. https://doi.org/10.1016/B978-0-443-15738-7.00026-X.

[3] Abdellatief TMM, Abdelkareem MA, Olabi AG. Green ammonia as a fuel: application. Comprehensive Green Materials 2025:466–78. https://doi.org/10.1016/B978-0-443-15738-7.00059-3.

[4] Menefee AH, Schwartz BA. Comparing green hydrogen and green ammonia as energy carriers in utility-scale transport and subsurface storage. Energy Clim Change 2024;5:100163. https://doi.org/10.1016/J.EGYCC.2024.100163.

[5] Makhlof MEM, Zabady AH, Shehata N. Green ammonia and the sustainable development goals (SDGs). Comprehensive Green Materials 2025:545–55. https://doi.org/10.1016/B978-0-443-15738-7.00080-5.

[6] Lin L, Lin Z, Xia Q, Qiu H, Sajid Khan M, Jin W, et al. Full-spectrum solar energy utilization for green ammonia production via solid oxide electrolysis cell coupled with haber-Bosch process. Energy Convers Manag 2024;310:118488. https://doi.org/10.1016/J.ENCONMAN.2024.118488.

[7] Bianchi FR, Bosio B. Modelling of green ammonia production based on solid oxide cells as electrolyser and oxygen separator for Haber-Bosch loop decarbonization. Int J Hydrogen Energy 2024;95:1183–93. https://doi.org/10.1016/J.IJHYDENE.2024.07.047.

[8] Zhou J, Tong B, Wang H, Xu G, Zhang R, Zhang W. Flexible design and operation of off-grid green ammonia systems with gravity energy storage under long-term renewable power uncertainty. Appl Energy 2025;388:125629. https://doi.org/10.1016/J.APENERGY.2025.125629.

[9] Nayak-Luke R, Bañares-Alcántara R, Wilkinson I. "Green" ammonia: impact of renewable energy intermittency on plant sizing and levelized cost of ammonia. Ind Eng Chem Res 2018;57:14607–16. https://doi.org/10.1021/ACS.IECR.8B02447.

[10] Wang C, Walsh SDC, Longden T, Palmer G, Lutalo I, Dargaville R. Optimising renewable generation configurations of off-grid green ammonia production systems considering Haber-Bosch flexibility. Energy Convers Manag 2023;280:116790. https://doi.org/10.1016/J.ENCONMAN.2023.116790.

[11] Liang X, Tang Y, Peng S, Wang X, Tang J, Liu H, et al. Techno-environmental-economic assessment of green ammonia production system integrated with off-grid offshore wind power. Int J Hydrogen Energy 2025;184:151902. https://doi.org/10.1016/J.IJHYDENE.2025.151902.

[12] Gu Y, Lan W. Optimal sizing of a wind-powered green ammonia plant for maritime fuel supply—A case in the greater Bay area. Energies 2025;18:18. https://doi.org/10.3390/EN18195157. 2025.

[13] Wu M, Fang J, Yan R, Zhang J, Cui S, Zhang Y, et al. Techno-economic analysis of hydrogen-to-power, ammonia-to-power pathway with biomass-to-power integration. Appl Energy 2026;407:127327. https://doi.org/10.1016/J.APENERGY.2025.127327.

[14] Poletto C, Dumont O, De Pascale A, Lemort V, Ottaviano S, Thomé O. Control strategy and performance of a small-size thermally integrated carnot battery based on a Rankine cycle and combined with district heating. Energy Convers Manag 2024;302:118111. https://doi.org/10.1016/J.ENCONMAN.2024.118111.

[15] Dumont O, Lemort V. Mapping of performance of pumped thermal energy storage (Carnot battery) using waste heat recovery. Energy 2020;211:118963. https://doi.org/10.1016/J.ENERGY.2020.118963.

[16] Laterre A, Dumont O, Lemort V, Contino F. Extended mapping and systematic optimisation of the Carnot battery trilemma for sub-critical cycles with thermal integration. Energy 2024;304:132006. https://doi.org/10.1016/J.ENERGY.2024.132006.

[17] Iqbal Q, Fang S, Xu Z, Yao Y, Song J, Qiu L, et al. Techno-economic comparison of high-temperature and sub-ambient temperature pumped-thermal electricity storage systems integrated with external heat sources. J Energy Storage 2024;89:111630. https://doi.org/10.1016/J.EST.2024.111630.

[18] Iqbal Q, Fang S, Zhao Y, Yao Y, Xu Z, Gan H, et al. Thermo-economic assessment of sub-ambient temperature pumped-thermal electricity storage integrated with external heat sources. Energy Convers Manag 2023;285:116987. https://doi.org/10.1016/J.ENCONMAN.2023.116987.

[19] Shamsi SSM, Barberis S, Maccarini S, Traverso A. Thermo-economic performance evaluation of thermally integrated Carnot battery(TI-PTES) for freely available heat sources. J Energy Storage 2024;97:112979. https://doi.org/10.1016/J.EST.2024.112979.

[20] Kurşun B, Ökten K. Improving the thermo-economic performance of a pumped thermal electricity storage (PTES) with a hybrid thermal integration scenario consisting of solar energy and waste heat. J Energy Storage 2024;103:114223. https://doi.org/10.1016/J.EST.2024.114223.

[21] Zhang M, Shi L, Hu P, Pei G, Shu G. Carnot battery system integrated with low-grade waste heat recovery: toward high energy storage efficiency. J Energy Storage 2023;57:106234. https://doi.org/10.1016/J.EST.2022.106234.

[22] Huang J, Zhao Y, Song J, Wang K, Zhu P, Liu B, et al. Thermodynamic investigation of a joule-Brayton cycle Carnot battery multi-energy system integrated with external thermal (heat and cold) sources. Appl Energy 2025;377:124652. https://doi.org/10.1016/J.APENERGY.2024.124652.

[23] Qi M, Cui C, Yu H, He T, Zhao D. Synergies between Carnot battery and power-to-methanol for hybrid energy storage and multi-energy generation. J Clean Prod 2023;430:139548. https://doi.org/10.1016/J.JCLEPRO.2023.139548.

[24] Marques da Cunha M, Petrollese M, Farinelli E, Morea D, Leonzio G. Performance analysis of bio-methanol production through bi and tri-reforming processes integrated into a Carnot battery. Energy 2025;335:138104. https://doi.org/10.1016/J.ENERGY.2025.138104.

[25] Smith C, Hill AK, Torrente-Murciano L. Current and future role of Haber–Bosch ammonia in a carbon-free energy landscape. Energy Environ Sci 2020;13:331–44. https://doi.org/10.1039/C9EE02873K.

[26] Zhou K, Cao Y, Si F. Thermodynamic optimization of integrated green ammonia-coal co-firing system with ScCO2 cycle. Appl Therm Eng 2025;279:127742. https://doi.org/10.1016/J.APPLTHERMALENG.2025.127742.

[27] Anwar M, Mehdizadeh AF, Karimi N. Waste heat recovery from a green ammonia production plant by Kalina and vapour absorption refrigeration cycles: a comparative energy, exergy, environmental and economic analysis. Sustain Energy Technol Assessments 2024;69:103916. https://doi.org/10.1016/J.SETA.2024.103916.

[28] Miyahira K, Aziz M. Hydrogen and ammonia production from low-grade agricultural waste adopting chemical looping process. J Clean Prod 2022;372:133827. https://doi.org/10.1016/J.JCLEPRO.2022.133827.

[29] Aziz M, Oda T, Morihara A, Kashiwagi T. Combined nitrogen production, ammonia synthesis, and power generation for efficient hydrogen storage. Energy Proc 2017;143:674–9. https://doi.org/10.1016/J.EGYPRO.2017.12.745.

[30] Mucci S, Stumm MD, Rix MJ, Mitsos A. Model-based evaluation of ammonia energy storage concepts at high technological readiness level. Appl Energy 2025;377:124495. https://doi.org/10.1016/J.APENERGY.2024.124495.

[31] Asgharian H, Duran AP, Yahyaee A, Pignataro V, Nielsen MP, Iov F, et al. Sustainable urea production via CO2 capture from cement plants: a techno-economic analysis with focus on process heat integration and electrification. Int J Hydrogen Energy 2025;151:150154. https://doi.org/10.1016/J.IJHYDENE.2025.150154.

[32] Hoxha J-L, Donceel A, Philippart de Foy M, Léonard G, Caspar M, Fraselle J, et al. Feasibility study of low-carbon ammonia and steel production in Europe. Eceee Industrial Summer Study Proceedings. 2020. https://orbi.uliege.be/handle/2268/250519.

[33] Frate GF, Ferrari L, Desideri U. Techno-economic comparison of Brayton pumped thermal electricity storage (PTES) systems based on solid and liquid sensible heat storage. Energies 2022;15:15. https://doi.org/10.3390/EN15249595. 2022.

[34] de la Hera G, Ruiz-Gutiérrez G, Viguri JR, Galán B. Flexible green ammonia production plants: small-scale simulations based on energy aspects. Environments 2024;11:11. https://doi.org/10.3390/ENVIRONMENTS11040071. 2024.

[35] Tully Z, King J, Johnson K. Hydrogen storage minimization under industrial flexibility constraints: a techno-economic analysis of off-grid green ammonia production. Int J Hydrogen Energy 2025;111:12–21. https://doi.org/10.1016/J.IJHYDENE.2025.02.109.